The Life Cycle of Upper-Level Troughs and Ridges: A Novel Detection Method, Climatologies and Lagrangian Characteristics

Sebastian Schemm [1] and Michael Sprenger [1]

[1]Institute for Atmospheric and Climate Science, ETH Zurich, Zurich, Switzerland

Correspondence: Michael Sprenger (michael.sprenger@env.ethz.ch)

Abstract. A novel method is introduced to identify and track the life cycle of upper-level troughs and ridges. The aim is to close the existing gap between methods that detect the initiation phase of upper-level Rossby wave development and methods that detect Rossby wave breaking and decaying waves. The presented method quantifies the horizontal trough and ridge orientation and identifies the corresponding trough and ridge axes. The trough and ridge axes allow us to study the dynamics of pre- and post-trough or ridge regions separately. The tracking allows us to study the temporal evolution of the trough or ridge orientation. The method is based on the curvature of the geopotential height at a given isobaric surface and is computationally efficient. First, the algorithm is introduced in detail, and several illustrative applications, such as a downstream development from the North Atlantic into the Mediterranean, and seasonal climatologies are discussed. For example, the climatological trough and ridge orientations reveal strong zonal and meridional asymmetry. Over land, most troughs and ridges are anticyclonically oriented, while they are cyclonically oriented over the main oceanic storm tracks. The cyclonic orientation increases towards the poles, while the anticyclonic orientation increases towards the equator. Trough detection frequencies are climatologically high downstream of the Rocky Mountains and over East Asia and Eastern Europe, but are remarkably low downstream of Greenland. Furthermore, the detection frequencies of troughs are high at the end of the Pacific storm track, but no comparable signal is seen over the North Atlantic. During El Niño-affected winters, troughs and ridges tilt anomalously strong cyclonically over North America and the North Atlantic, in agreement with previous findings based on traditional variance-based diagnostics such as **E** vectors. During La Niña the situation is essentially reversed. Finally, the identified troughs and ridges are used as starting points for 24-hour backward parcel trajectories, and a discussion of the distribution of pressure, potential temperature and potential vorticity changes along the flow path is provided to give insight into the three-dimensional nature of troughs and ridges.

1 Introduction

Troughs and ridges are ubiquitous flow features in the upper troposphere and are centerpieces of weather and climate research, and for good reason. In general, a trough is associated with cyclonic flow and pushing cold air equatorward. It is depicted as a region of reduced geopotential height on an isobaric surface or enhanced potential vorticity on an isentropic surface. The counterpart of a trough is a ridge, which is associated with warm air pushing poleward, enhanced geopotential height (corresponding to reduced potential vorticity [PV]) and anticyclonic flow. Jointly, a trough and a ridge form the positive and

negative phases, respectively, of large-scale Rossby wave patterns, which shape weather development. At the equatorial tip of a trough, where the geopotential isolines are closely aligned (or the PV gradient is at a maximum), a jet streak can form, and the conservation of the absolute vorticity and a region of diffluent flow in the jet exit region predict large-scale upward motion. It is therefore not too surprising that surface cyclogenesis (Petterssen and Smebye, 1971; Sanders, 1988; Lackmann et al., 1997;

5 Graf et al., 2017), rapid cyclone intensification (Sanders and Gyakum, 1980; Wash et al., 1988; Uccellini, 1990; Wernli et al., 2002; Gray and Dacre, 2006) and enhanced precipitation (Martius et al., 2006; Massacand et al., 2001; Martius et al., 2013) usually take place in the region ahead of the upper-level trough axis.

The shape and orientation of troughs and ridges is pivotal in determining their influence on synoptic-scale flow evolution. A trough, or a ridge, tilts cyclonically if it forms under cyclonic shear, while it acquires an anticyclonic orientation if it forms

10 under anticyclonic shear (Davies et al., 1991; Thorncroft et al., 1993). In the case of a pronounced equatorward (poleward) excursion of a trough (ridge), it may wrap up and undergo irreversible deformation in a wave breaking event (McIntyre and Palmer, 1983; Thorncroft et al., 1993). Under anticyclonic shear, the trough deforms into a narrow band, called a streamer, which extends equatorward to the mean jet position. During the associated wave breaking event, the jet is pushed poleward. With cyclonic shear, wave breaking occurs poleward of the mean jet position, thereby pushing the jet equatorward (Thorncroft

15 et al., 1993; Lee and Feldstein, 1996; Orlanski, 2003). This process, through which cyclonically or anticyclonically breaking troughs and ridges displace the jet, is even able to excite positive or negative North Atlantic Oscillation events (Benedict et al., 2004; Franzke et al., 2004; Rivière and Orlanski, 2007). A traditional means for quantifying the influence of upper-level troughs and ridges on the jet strength and location is the **E** vector (Hoskins et al., 1983; Trenberth, 1986). With anticyclonic shear, troughs and ridges acquire an anticyclonic orientation, and the **E** vector points equatorward, indicating poleward eddy

20 momentum flux. With cyclonic shear, a poleward-pointing **E** vector indicates southeast-to-northwest-oriented troughs and ridges, which correspond to a cyclonic orientation, and the corresponding equatorward eddy momentum flux pushes the jet equatorward (Hoskins et al., 1983; Rivière et al., 2003).

Troughs and ridges actively interact with diabatic processes and are far from being dry adiabatic flow features. Ahead of the trough axis, where vertical motion prevails, air from the surface warm sector of a cyclone is lifted within the warm conveyor belt

25 (WCB) to upper levels (Harrold, 1973; Browning, 1986, 1990; Wernli, 1997). During ascent, the air is diabatically modified, for example, by condensation, in a way that amplifies the upper-level ridge and the anticyclonic flow downstream of the surface cyclone (Stoelinga, 1996; Wernli and Davies, 1997; Grams et al., 2011; Schemm et al., 2013). This process also amplifies the streamer formation (Massacand et al., 2001) and accelerates the jet. From a PV perspective, this phenomenon is seen as a negative PV anomaly around the WCB outflow, corresponding to enhanced anticyclonic circulation, and by a sharpening of

30 the PV gradient along the edge of the WCB outflow, corresponding to an accelerated jet. From a momentum flux perspective, the center of the WCB outflow corresponds to a region of enhanced horizontal eddy momentum flux divergence (leading to a deceleration), and the edge of the WCB outflow corresponds to a region of enhanced eddy momentum flux convergence (leading to an acceleration) (Schemm, 2013). The WCB outflow ahead of an upper-level trough has thus been shown to accelerate downstream cyclone growth (Wernli and Davies, 1997; Pomroy and Thorpe, 2000; Grams et al., 2011; Schemm

35 et al., 2013) and can even lead to the formation of large-scale blocks (Pfahl et al., 2015; Steinfeld and Pfahl, 2019). Recent

studies have presented further evidence for the non-negligible role of turbulence and radiation in the diabatic modification of the life cycle of troughs and ridges (Spreitzer et al., 2019). The dynamics of troughs and ridges thus may act as a stepping stone towards a better understanding of the coupling between adiabatic and diabatic processes and allows for the connection of atmospheric processes from the planetary scale to the mesoscale.

5   In this study, a novel feature-based method is introduced for identifying and tracking the life cycle of upper-level troughs and ridges, including their axes and orientations in gridded data. Feature-based methods for detecting streamers and wave breaking events are widely used research tools, and the motivation behind this work is to extend the capability of available tools and to track and characterize the entire life cycle of upper-level troughs and ridges from genesis to lysis. We further aim to compare the detected life cycle characteristics of, for example, the trough orientation, with previous results obtained

10 from more traditional methods such as the aforementioned **E** vectors, thereby bridging gaps between different perspectives on synoptic-scale evolution.

    The paper is organized as follows. Details of the algorithm and a case study are presented in Section 2, and Section 3 is dedicated to the discussion of winter and summer climatologies, the change in the trough and ridge orientation during ENSO-affected winters and over the Pacific in midwinter. In Section 4, we explore troughs and ridges from a Lagrangian viewpoint

15 before concluding the paper in Section 5.

2   Data and Methods

The trough and ridge identification algorithm is based on 6-hourly ERA-Interim data (Dee et al., 2011). The reanalysis data are provided publicly by the European Centre for Mid-Range Weather Forecasts (ECMWF) via URL <apps.ecmwf.int/datasets>. More specifically, the identification is based on the 500-hPa geopotential height data, which are interpolated onto a regular

20 $1° \times 1°$ grid. The investigation period is 1979-2018, and the monthly mean trough and ridge climatologies are publicly available at URL <eraiclim.ethz.ch> (Sprenger et al., 2017).

    This section describes in detail how the trough and ridge axes are identified and tracked. Three distinct steps are involved:

– identifying 2D trough and ridge objects (masks) and their corresponding axes;

– tracking the trough and ridge objects and quantifying their age and overall lifetimes;

25 – characterizing the horizontal orientation of each trough and ridge axis.

The following subsections will address specific aspects of the algorithm, including a detailed validation.

2.1   Trough and Ridge Identification

The identification of troughs and ridges starts with the geopotential height at, for example, 500 hPa, as seen in Fig. 1a for 12 UTC on 12 January 2010. Two distinct troughs and one ridge can visually be identified: a northwest-to-southeast oriented

30 trough over the eastern North Atlantic, which is associated with a mature low pressure system to the west of Ireland; a meridionally oriented ridge, which extends from the Iberian Peninsula to the UK; and a meridionally oriented trough over the Central

Mediterranean to the southeast of Italy over the Ionian Sea. The goal of an automated trough and ridge detection is to automatically identify these features and the corresponding axes. Several aspects have to be kept in mind. First, the smooth geopotential isolines shown in Fig. 1a do not reflect the underlying $1° \times 1°$ ERA-Interim grid, but are already smoothed due to the contour drawing algorithm. Therefore, in the following panels (Fig. 1b to f), the geopotential height is shown on the underlying input

5   grid. Second, troughs and ridges may exhibit a complicated structure. For instance, the horizontal orientation varies along a trough or ridge axis; a trough or ridge can be broken into different segments; and the curvature of the geopotential isolines can considerably vary over small distances. The challenge for an automatic detection algorithm is to identify all these different characteristics. In the following, details of the proposed algorithm are described.

Geometrically, we suggest to identify troughs and ridge using the curvature of the geopotential isolines. To this end, the

10 change of the orientation of a vector pointing along an isoline is computed. First, at every grid point, the gradient of the geopotential field is calculated and the gradient vector is rotated by $90°$, such that the rotated vector aligns with the geopotential isolines. Next, a new location 5 km in the direction of the aligned vector is determined, and the corresponding aligned vector at this new location is obtained trough bilinear interpolation. Because of the curvature of the geopotential isolines, the original and the 5-km shifted vectors are rotated against each other, and it is the angle between these two vectors– normalized by the

15 distance of 5 km – that we define as the local curvature. The curvature field $\alpha(x,y)$ is available on the whole global grid and is used to identify the trough and ridge objects.

To identify troughs and ridges, a threshold of $5 \cdot 10^{-5}$ degree per meter is used to mask the curvature field (Fig. 1b). This threshold is the main degree of freedom of the algorithm. All connected points in the masked field, which form a coherent object, are clustered into one distinct 2D trough or ridge depending on the sign of the curvature field (Fig. 1c). We selectively

20 disregard very small features ($< 20 \cdot 111^2$ km^2), which at this stage unlikely correspond to a significant flow deviation. Additionally, consideration is only given to midlatitude troughs and ridges within $20°$S–$70°$N, but the algorithm in general could be applied also to polar latitudes. Figure 1 illustrates the individual steps. Figure 1b shows the trough and ridge objects after masking the normalized curvature field using the above threshold. The trough over the eastern North Atlantic is connected to a mature low-pressure system, which is discernible from the closed 500-hPa isolines in the upper-left corner of Fig. 1a. This

25 trough is classified as a "closed trough". On the other hand, the trough object over the Central Mediterranean is not associated with a low-pressure system and is therefore classified by the algorithm as an "open trough". We decided to classify regions inside closed geopotential contours not as part of a trough or ridge object, as is the case for the trough over the Atlantic in Fig. 1b, but rather flag the region inside a closed geopotential contour as a distinct low- or high-pressure systems as in Sprenger et al. (2017). In this way, troughs and ridges can be classified as either independent of or as linked with a low- or high-pressure

30 system and the troughs and ridges are classified as such by the algorithm.

In a final step, the corresponding trough and ridge axes are identified. The result of this step is shown in Fig. 1d. Algorithmically, a starting point is first selected within each 2D trough and ridge object, and we decided to start at the highest (for troughs) and lowest (for ridges) geopotential value within each object. From this starting point, a line is iteratively constructed by stepping 5 km forward parallel to the geopotential gradient. The iterative extension of the axis line ends as soon as the line

35 leaves the 2D trough or ridge object. If the identified axis is shorter than 500 km, the axis and the corresponding 2D trough or

trough and ridge identification is therefore a gridded field, corresponding to the original input grid, on which trough and ridge
grid cells are labelled and flagged in different ways (e.g., open or closed). For plotting purposes, it is convenient to transform
the axes into 1D polylines by means of a cubic-spline interpolation (as is done in Fig. 1e,f).

5   The troughs and ridges are further characterized with respect to their horizontal orientation. The horizontal orientation
(or tilt) of a trough or ridge differs from the curvature of the geopotential isolines. To obtain the horizontal orientation, the
angle of the trough or ridge axis is estimated relative to a north-south meridian at every grid point and projected laterally to
the whole 2D object. We refrain from attributing an unique orientation to the entire 2D trough or ridge object. Instead, the
orientation can change, or even reverse its sign, along the axis of a trough or ridge. An example is shown in Fig. 1f. A positive
10 angle corresponds to a southwest-northeast orientation (anticyclonic) and negative values to a southeast-northwest orientation
(cyclonic) and the orientation can change within the same object. Near-zero values correspond to meridionally oriented troughs
and ridges. For instance, the southeast-northwest oriented trough in the North Atlantic is tilted cyclonically by 30–45° relative
to the north-south meridians (Fig. 1f). On the other hand, the ridge to the south of the UK is very weakly tilted relative to the
meridians, and marginally changes its orientation from its northern to its southern tip. The easternmost trough over the Central
15 Mediterranean has a mild anticyclonic orientation (blue shading in Fig. 1f).

Finally, we apply a tracking algorithm to determine the age and overall lifetime of the individual trough and ridge objects.
An example is shown in Fig. 1e, where the trough over the eastern North Atlantic is found to be rather young (6–12 h), but
still a little older (0–6 h) than the trough over the Central Mediterranean. The ridge to the south of the UK is about 18-24 h
old. Algorithmically, the tracking determines spatio-temporally connected trough and ridge objects by applying an overlap
20 criterion. Further details can be found in (Rüdisühli, 2018). The tracking can be used, for example, to study the change in the
orientation of the troughs and ridges during their life cycle.

2.2   Illustrative case: Downstream development over the North Atlantic–Mediterranean sector

In the section, an illustrative example is briefly discussed. Figure 2 compares two distinct time instances (06 UTC and 12 UTC
on 12 January 2010, in Fig. 2a and b, respectively) for a synoptic evolution over the eastern North Atlantic–Mediterranean
25 sector. At 06 UTC on 12 January 2010 (Fig. 2a), a trough, which is connected to a mature low-pressure system over the
eastern North Atlantic, is located near 20°W. Quasi-geostrophic (QG) forcing for downward motion is found upstream (yellow
contours in Fig. 2) of the trough axis, and forcing for upward motion on its downstream side (green contours in Fig. 2). The
quasi-geostrophic forcing is computed at 500 hPa according to the Q-vector formulation of the classical quasi-geostrophic
omega equation [details of this computation are given in the supplement to Graf et al. (2017)]. The identified trough axis sits
30 in the transition zone between downward and upward forcing, thus highlighting the physical relevance of the identified axis
and therefore could be used to separate the pre-trough sector from the post-trough sector. A downward and upward QG-forcing
pattern is also discernible over the Central Mediterranean, but a corresponding trough axis is missing at 06 UTC (Fig. 2a), which
is related to the degree of freedom the user has in setting the minimum curvature and length of the axis. Six hours later at 12
UTC (Fig. 2b), the trough axis is identified and located in between the upward and downward forcing. Overall, the temporal

evolution of the synoptic situation is reminiscent of the situations discussed by Raveh-Rubin and Flaounas (2017). It seems to follow a common pattern for Mediterranean cyclogenesis. The outflows of warm conveyor belts from upstream cyclones over the Atlantic Ocean tend to amplify a ridge over the eastern Atlantic. The consequent downstream wave development intrudes the Mediterranean in southern latitudes and provokes cyclogenesis. Interestingly here it is a trough over the North

5 Atlantic and the ridge downstream already exists for a longer time period than the up- and downstream troughs. This tends to be in agreement with the finding in Raveh-Rubin and Flaounas (2017) that a series of Atlantic cyclones is necessary to initiate Mediterranean cyclogenesis. The trough and ridge tracking could therefore be used to quantify the time between the formation of the upstream Atlantic trough, the downstream ridge and the downstream Mediterranean trough plus the typical orientation of these features preceding Mediterranean cyclogenesis.

10 **3 Climatologies**

In this section, the trough and ridge diagnostics presented above are applied to compute climatologies for the extended winter (Nov–Mar) and summer (May–Sep) seasons in the Northern Hemisphere. We restrict the discussion for practical reasons to the extended winter and summer seasons, as we intend to present an in-depth discussion of the monthly and seasonal cycles in both hemispheres in future publications.

15 **3.1 Extended Winter (November–March)**

In Fig. 3a, a summary is given for the frequency of trough detection, the averaged trough age (yellow and red contours in Fig. 3a), and the mean horizontal orientation (Fig. 3b) on the 500 hPa level. During winter, the trough detection frequency displays four centers of action around the Northern Hemisphere, for example, over North America downstream of the Rocky Mountains and over East Asia downstream of the Atlai-Sayan and Yablonoi mountain ranges. The trough detection frequency

20 also peaks at the end of the North Pacific storm track over the Bay of Alaska and over Eastern Europe slightly to the north of the Black Sea. The latter maximum has an upstream branch into the Mediterranean and a downstream branch into the Caspian Sea. Surprisingly, and in contrast to the Rocky Mountains, there is no peak downstream of Greenland, which is an important surface cyclogenesis region. Greenland surface cyclogenesis is typically preceded by an eastward propagating upper-level trough-ridge train, which is seen, for example, in Fig. 4 of Schemm et al. (2018). Because detection frequencies tend to highlight regions

25 where troughs are stationary, it seems as if troughs downstream of Greenland are more transient compared to their counterparts downstream of the Rocky Mountains. Furthermore, there is no center of action over the Nordic Seas, which is one exit region of the North Atlantic storm track. This is in contrast to the exit of the Pacific storm track and the maximum over the Bay of Alaska.

The mean trough age is obtained using the tracking capability of the algorithm (section 2). Early troughs, with an age

30 between 0 and 1 day (yellow contour in Fig. 3a), are most frequently detected downstream of the Rocky Mountains and over East Asia downstream of the Yablonoi mountain range, suggesting that these two regions are preferred trough genesis regions. There is also a smaller peak in the early trough frequency near Greenland, suggesting that trough genesis also occurs

in Greenland. However, the reduced trough frequency compared to the Rocky Mountains suggests that Greenland troughs are indeed more transient. A second small peak of early troughs is seen in the Gulf of Genoa, a preferred surface cyclogenesis region for Mediterranean cyclones. There are two broader regions where early troughs are frequent. The end of the storm track over the North Pacific and over parts of Northern Europe encompasses a broader region that extends from the UK eastward

5 across Europe into Russia. It is plausible to think of these early troughs over Europe as a result of synoptic systems that decay upstream over the Eastern North Atlantic. Wave breaking and consecutive downstream developments at the end of a synoptic wave life cycle over the Eastern North Atlantic provide the seed for trough genesis further downstream over Europe. A note of caution regarding the climatological trough age must be mentioned: to obtain the age climatology, the age information obtained from trough tracking is assigned to every grid point inside a two-dimensional trough feature. All the grid points outside a

10 trough feature are labeled as missing data. Time averaging results in the mean age at each grid point. The climatological age is therefore a function of the trough size, and the age contours therefore enclose smaller regions everywhere where troughs tend to be small. Furthermore, the number of troughs at each grid point varies according to the trough frequency (color shading in Fig. 3a), and near the lateral boundaries of the domain, a very low number of troughs dictates the climatological mean. Late-trough frequencies typically encompass larger regions and extend downstream (not shown), but the absolute frequency

15 values are considerably reduced.

The trough orientation displays a strong zonal asymmetry. Over the main oceanic storm tracks, the mean trough orientation is preferentially cyclonic (blue shading in Fig. 3b). The cyclonic orientation increases towards the end of the storm tracks and increases with latitude. Over land, the trough orientation is preferentially anticyclonic. The anticyclonic orientation increases towards lower latitudes. This meridional dependence of the mean trough orientation is in agreement with the conventional

20 interpretation of cyclonic and anticyclonic wave life cycles and the associated wave breaking, which occurs poleward (cyclonic) or equatorward (anticyclonic) of the mean jet position (Thorncroft et al., 1993). Over Northern Africa, the climatological trough orientation is strongly anticyclonic. In this region, troughs are frequently associated with anticyclonic waves breaking downstream of a mature extratropical cyclone situated off the Iberian Peninsula. This downstream trough eventually thins and elongates equatorward, corresponding to streamer formation. Eventually, an upper-level cutoff low will form later. From the

25 perspective of Rossby wave packets propagating along wave guides, the anticyclonic troughs in this sector have been described as the transmitters between wave packets initiated on the subtropical wave guide (i.e., the jet over Northern Africa) by wave packets that propagate along the extratropical wave guide over the North Atlantic (Martius et al., 2010, ;in particular Fig. 5).

In Fig. 4a, a summary is given for the number of ridges detected during the cold season. Remarkably, the ridge detection frequency over many regions is larger by almost a factor of two compared to the trough detection frequency. For example, the

30 ridge detection frequency downstream of Greenland with a preferred cyclonic orientation (Fig. 4b) is as twice as high as that for troughs. The band of enhanced ridge frequencies elongates downstream over the Nordic Seas, peaks over the Scandinavian Mountains and remains on a relatively high level over Siberia. Upstream of the Atlai-Sayan and Yablonoi Mountains, the ridge frequency decreases; while downstream, the trough frequency peaks (Fig. 3a). Over large parts of Siberia, the ridges have no preferred orientation, while they tend to be anticyclonically oriented over East Asia. This band of higher ridge frequencies

35 might relate to the Siberian storm track, seen in the track densities of 250-hPa meridional wind anomalies (Fig. 4a in Hoskins

and Hodges, 2019), while the main surface storm track is located further poleward over the Barents Sea region (Fig. 4a Wernli and Schwierz, 2006). Over East Asia and the West Pacific, the ridge detection frequency is rather low, while the climatology is dominated by stationary ridges over the Coast Mountains of western North America, which preferentially have a cyclonic orientation (blue shading in Fig. 4b). A smaller region of high early-age trough frequencies is found near Kamchatka (yellow

5 contour in Fig. 4a), which indicates the presence of a transient ridge with a preferred cyclonic orientation (blue shading in Fig. 4b). Indeed, a local maximum in the surface cyclone frequencies is found downstream of Kamchatka (see Fig. 4a in Wernli and Schwierz, 2006). Overall, the trough and ridge pattern alternates almost periodically in terms of the amplitude around the Northern Hemisphere.

3.2 Extended Summer (May–September)

10 The pattern in the trough detection frequencies changes from winter to summer (Fig. 3c). Over North America, the main frequency peak is located downstream of the Great Lake Region and over Newfoundland, while it was previously located further upstream. This is in agreement with the high surface cyclone frequencies seen in summer in this region (see Fig. 4c in Wernli and Schwierz, 2006). Over the North Atlantic, the main frequency peak is located just off the Iberian Peninsula. There is no comparable peak in surface cyclone frequencies in this region. Surface cyclone frequencies have a peak downstream of

15 Greenland (see Fig. 4c in Wernli and Schwierz, 2006); however, there is no maximum trough frequency. However, upper-level storm-track measures, based on, for example, track densities of 250 hPa vorticity, indeed indicate the presence of a trough-like feature off the Iberian Peninsula during summer (see Fig. 1c in Hoskins and Hodges, 2019). Because a similar feature is also seen in summertime climatologies of Rossby wave breaking (see Fig. 10a in Postel and Hitchman, 1999), we expect this maximum in trough frequency to be related to anticyclonic Rossy wave breaking as described for the LC1 scenario in Fig. 12a

20 of Thorncroft et al. (1993). An example of such a synoptic situation is also shown in Fig. 5.7 of Martius and Rivière (2016).

  Over Eurasia, one maximum in the summertime detection frequencies of troughs connects the Eastern Mediterranean with the Black Sea. This feature is not well reproduced in Rossby wave breaking climatologies of which we are aware, but it is clearly seen in the upper-level track densities in vorticity on 250 hPa (Hoskins and Hodges, 2019). Furthermore, this local maximum corresponds to a similar maximum seen in summertime climatologies of stratospheric streamers (see Fig. 6b in Wernli and

25 Sprenger, 2007). Streamers form a subcategory of troughs and are best described as filament-like elongated troughs, which have a length that is longer than their width (Wernli and Sprenger, 2007). Streamers are associated with anticyclonic Rossby wave breaking, so it is not too surprising that the detection hot spots off the Iberian Peninsula and near the Black Sea eventually become part of the same Rossby wave train [see for example Fig. 3 in (Wernli and Sprenger, 2007) for such a synoptic situation]. A second maximum over Eurasia is located near Lake Baikal, a feature seen again in the streamer climatology of

30 Wernli and Sprenger (2007). Further east, the maximum over East Asia exhibits only weak changes in its location between winter (Fig. 2a) and summer (Fig. 2c) but appears with a reduced amplitude during summer. Finally, over the East North Pacific, the summer maximum is located slightly equatorward compared to its position during winter. It is located off the West Coast of the US during summer, while it is located in the Bay of Alaska during winter. This is a counterintuitive result because storm tracks generally tend to shift poleward during summer (Hoskins and Hodges, 2019).

The ridge frequency pattern over North America continues to be dominated by the stationary ridges over the Coastal Mountains despite a mild reduction in the absolute detection values (color shading in Fig. 4c).

3.3 ENSO-affected winter seasons

The influence of the El Niño–Southern Oscillation (ENSO) on the midlatitudes is a longstanding research topic – for recent reviews, we refer the reader to publications by Liu and Alexander (2007); Stan et al. (2017) and Yeh et al. (2018). Recently, progress has particularly been made in understanding the role of synoptic-scale eddies in shaping the North Atlantic circulation response to ENSO. More specifically, there is increasing evidence that the North Atlantic teleconnection pattern is in part a downstream response of the eddy-driven jet to changes in the orientation of synoptic-scale eddies entering the North Atlantic from North America (Li and Lau, 2012a, b; Drouard et al., 2015). The mechanisms can be briefly summarized as follows – for a schematic summary see also Fig. 13 in Schemm et al. (2018): In response to an amplified ridge over the northeastern Pacific during La Niña, upper-level synoptic eddies with a more anticyclonic orientation form downstream of the Rocky Mountains, where lee cyclogenesis is enhanced. These eddies propagate downstream over the North Atlantic while maintaining their anticyclonic orientation until anticyclonic wave breaking occurs over the North Atlantic. Anticyclonic wave breaking pushes the eddy-driven jet poleward. Until now, the anomalous anticyclonic orientation and the associated more poleward eddy momentum flux were diagnosed using the **E** vectors of Hoskins et al. (1983), which are obtained using high-pass filtered wind data. As summarized in the introduction, equatorward-pointing **E** vectors are assumed to indicate anticyclonically oriented eddies (Rivière et al., 2003) associated with a more poleward eddy momentum flux. During El Niño, the situation is essentially the opposite: Eddies downstream of the Rocky Mountains exhibit a more cyclonic tilt and tend to push the North Atlantic jet equatorward, as is suggested by more poleward-oriented **E** vectors. The Pacific and North Atlantic jets are more zonally extended, which tends to increase extratropical cyclogenesis over the Gulf Stream (Schemm et al., 2016). To shed further light on this, we therefore explore the ENSO climatologies using trough and ridge detection, which are very closely related to the upper-level eddies described above.

In Fig. 5, anomalies in the orientation of troughs and ridges are shown for ENSO-affected winter seasons based on the Oceanic Niño Index (ONI) from NOAA's Climate Prediction Center. During El Niño (Fig. 5a), troughs and ridges exhibit a stronger cyclonic orientation over the northeastern North Pacific, North America and over the North Atlantic. The anomalies are strongest over the northeastern Pacific off the East Coast of the US. Over the North Atlantic, the stronger-than-usual cyclonic orientation is most pronounced along 30°N, which is about the latitude of the zonally more extended jet in this region during El Niño. In contrast, during La Niña, troughs and ridges exhibit a more anticyclonic orientation over the eastern North Pacific, North America and parts of the North Atlantic. These results are in agreement with those from previous studies, which rely on the strength and orientation of the **E** vectors. The trough and ridge detection and tracking algorithm can thus enrich insights into the dynamics of upper-level eddies during ENSO-affected winters. For example, the anomalies during El Niño over the northeastern Pacific are predominantly due to more cyclonically oriented troughs, while the anomalies over the North Atlantic have a stronger signal in the ridge anomalies (not shown). The more cyclonic trough and ridge orientation over the Pacific is

connected to the deepening of the Aleutian Low during El Niño, whereas it is a strong Aleutian *High* during La Niña, which is in agreement with more anticyclonic troughs and ridges (Mo and Livezey, 1986).

3.4 The North Pacific storm track in midwinter

The midwinter suppression of the North Pacific storm-track intensity is another research topic that has recently received re-
5   newed attention. While the mean baroclinicity is largest during midwinter, storm track activity is reduced over the North Pacific, in contrast to the North Atlantic (Nakamura, 1992). Feature-based tracking statistics have shown that suppression is connected to a reduced eddy intensity and upper-level eddy frequency (Penny et al., 2010), while it does not affect the frequency of surface eddies (Schemm and Schneider, 2018). Several mechanisms are suggested to contribute to the suppression. For example, a reduction in upstream seeding was strongly debated (Penny et al., 2010; Chang and Guo, 2011; Penny et al.,
10 2011; Chang and Guo, 2012; Penny et al., 2013), as well as an increase in the jet speed and a concomitant reduction in the jet width (Harnik and Chang, 2004). Recently, however, several studies have highlighted the important role of processes internal to the North Pacific storm track, such as a reduction in the lifetime of eddies (Schemm and Schneider, 2018) and an increase in the eddy group velocity (Chang, 2001). There is growing evidence that the equatorward shift in the subtropical jet is key for understanding suppression (Chang, 2001; Nakamura and Sampe, 2002; Yuval et al., 2018; Schemm and Rivière, 2019). When
15 the subtropical jet over the Pacific shifts equatorward, the efficiency of synoptic systems to convert the mean baroclinicity into eddy energy is reduced due to a change in the vertical eddy structure (Chang, 2001; Schemm and Rivière, 2019). The vertical eddy structure, which is more poleward when the eddy efficiency decreases during midwinter, is constrained by the eddy propagation direction, which is more towards the equator during midwinter (Schemm and Rivière, 2019; Novak et al., 2020); see, for example, Figs. 1 and 8 in Schemm and Rivière (2019). Equatorward jet shifts also reduce the storm-track intensity over
20 the North Atlantic (Penny et al., 2013; Afargan and Kaspi, 2017) and even in idealized aqua-planet simulations (Novak et al., 2020).

The equatorward shift of the Pacific jet changes the large-scale environment in which synoptic systems grow because more systems will now grow on the poleward flank of the jet. The poleward flank is characterized by a large-scale cyclonic-sheared environment. According to idealized wave life cycles (Thorncroft et al., 1993), we must expect more cyclonic (LC2) develop-
25 ments during midwinter. Indeed, troughs and ridges at the 500-hPa level exhibit a stronger cyclonic orientation during January (Fig. 6b) compared to, for example, November and April (Fig. 6a,c). Not only increases the mean cyclonic orientation during midwinter but also wider parts of the Pacific are now affected by cyclonically oriented troughs and ridges. In particular, during January, cyclonic troughs dominated the North Pacific even equatorward of 40°N, which is not the case during November and April.

30 There are several observations based on trough and ridge detection that may prove useful in gaining a better understanding of midwinter suppression. First, there is no marked reduction in the number of troughs and ridges during midwinter, which, however, is the case for bandpass-filtered eddies at the same height (Penny et al., 2010). Second, there is basin-wide dominance of cyclonically oriented troughs (and, to a lesser extent, ridges) during midwinter, with two maxima over the eastern Pacific and western Pacific (right column in Fig. 6b), which indicates a consistent change in the character of synoptic wave life cycles

during midwinter. The first maximum between 40–50°N, 165°–180°E is colocated with the region of maximum reduction in the efficiency of baroclinic growth (see Fig. 2b in Schemm and Rivière, 2019) and slightly upstream of the maximum eddy kinetic energy (see Fig. 1 in Schemm and Schneider, 2018), which is suppressed during midwinter. Because the cyclonic orientation of troughs and ridges is typically strongest during the final stage of a synoptic wave life cycle, a plausible, but here untested, hypothesis for the existence of the first maximum would be that synoptic cyclones generated east of Japan over the Kuroshio extension have an accelerated life cycle with a fast and intense deepening phase followed by a rapid decay. Thus, the conversion rates and EKE are reduced downstream of the maximum cyclonic orientation of the upper-level troughs compared to the shoulder seasons. Indeed, a reduction in the lifetime of synoptic systems is observed during midwinter (Schemm and Schneider, 2018). The second maximum is related to the decay of the synoptic waves at the exit of the Pacific storm track in the Bay of Alaska.

4   Lagrangian perspective on troughs and ridges

In this section, we show how trough and ridge detection can be used to investigate trough and ridge dynamics from a Lagrangian perspective. To this end, we couple the trough and ridge detection tool with the Lagrangian analysis tool LAGRANTO [Wernli and Davies (1997); Sprenger and Wernli (2015)], which we use to compute parcel trajectories from detected trough and ridge features.

The procedure is best explained using a simple example. At 18:00 UTC on 18 Jan 2010, a trough is detected over the Nordic Seas downstream of a mature low-pressure system south of Greenland (Fig. 7a). The trough has a mild cyclonic orientation and will broaden during the following days. A potential research question would be: Is the formation of this downstream trough predominately driven by dry dynamics or considerably modified by diabatic processes? Parcel trajectories are released from every grid point inside the trough feature (thin gray lines in Fig. 7a), which highlight the pathway of air parcels that constitute the trough at the 500-hPa level. The mean evolution of pressure (Fig. 7b) and potential vorticity (Fig. 7c) along these parcel trajectories suggests that the air is mostly advected horizontally with only small diabatic modification of the potential vorticity during the 24 hours prior to arrival in the target region. The potential temperature decreases during this period only marginally from 297 to 295 K. Thus, the dynamics underlying the formation of this specific downstream trough are, at this stage of its life cycle, mostly dry and therefore can be understood by the traditional paradigm of downstream development (Simmons and Hoskins, 1979; Orlanski and Chang, 1993; Simmons, 1994; Papritz and Schemm, 2013).

Next, 24-hour backward trajectories are released from all the detected troughs and ridges over the North Atlantic (60°–0°W, 20–70°N) in one winter (January 2010) and in one summer month (July 2010). During January 2010, more than 25,000 parcel trajectories are released, and during July 2010, more than 16,000 parcel trajectories. The binned 24-hour changes for pressure and potential vorticity are presented in Fig. 8. During January 2010, the distribution of 24-hour pressure changes is centered between 0-100 hPa (corresponding to a weak descent) and is highly skewed towards negative values (corresponding to a strong ascent) of up to -500 hPa, while positive values are capped at 250 hPa. This phenomenon reflects the nature of the mean isentropic motion inside troughs in which equatorward pushing air mildly descends due to isentropic downglide,

while for some cases vigorous vertical motions occur, which is in agreement with the long tail towards positive values of the potential temperature distribution (Fig. 8e,f,). The trajectories associated with strong vertical motion all originate in the boundary layer and first increase and later decrease their potential vorticity (not shown), which is characteristic of a warm conveyor belt ascending ahead of the trough axis (e.g., Wernli and Davies, 1997). These cases exhibit a marked increase in

5 potential temperature, which reflects the cross-isentropic motion. For the few cases with a strong decrease larger than 200 Pa in 24 hours, we find that the vast majority most of the parcels, which originate from levels between 200 and 300 hPa, decrease their potential vorticity. Only a small fraction of approximately 1% starts with stratospheric values (>2 pvu[1]), but we assume that this number increases for 300-hPa troughs. The binned 24-hour changes of potential temperature are centered between -2 and 0 K. Most of these air parcels are associated with only a mild change in pressure. Our interpretation is that the reduction in

10 potential temperature is due to radiative cooling, but a detailed analysis of all diabatic tendencies would be needed to confirm this result. Finally, we note that the 24-h pressure change for July is even more confined to values between 0 and 100 hPa, while the 24-h change in potential vorticity is more confined between -0.2 and 0.2 pvu, which is a result that reflects the overall more intense cyclone and associated trough-ridge development and vertical motion during winter.

For the 500-hPa ridges, the histogram of changes in pressure along the flow of 24-hour backward parcel trajectories is

15 centered between -100 and 0 hPa with a longer tail towards negative values. It is therefore shifted more towards negative values than the trough histogram, which reflects the isentropic upglide of air sliding poleward and upward in a ridge. The pressure change during July is again more shifted towards negative values (ascent) than the trough histogram but is centered around -50–50 hPa. If our interpretation is correct, the histograms are dominated by the mean mostly dry isentropic motion of air inside troughs and ridges, and the reduced pressure change along the flow in July relative to January reflects the reduced baroclinicity

20 or isentropic tilt in summer compared to winter. The histograms of potential vorticity changes are symmetrically distributed around zero with outliers on both sides of the spectrum, while the distribution of the 24-hour potential temperature changes are centered around week negative values (-2 to 0 K), which is similar to the troughs.

5 Conclusions

In this paper, a novel method to detect the full life cycle of upper-level troughs and ridges is presented, which is computationally

25 efficient and closes an existing gap between tools that focus either on the wave breaking phase or on the initiation phase of upper-level Rossby waves. The presented approach is based on the curvature of the geopotential isolines at a given isobaric surface. Grid points above a predefined curvature value are grouped into two-dimensional features and labeled as trough or ridge features. The algorithm further categorizes the corresponding trough and ridge axes as line objects and identifies the horizontal orientation. It also performs a spatio-temporal tracking of the identified features. The detection of the trough and

30 ridge axes allows for the identification of pre- and post-trough or ridge sectors, respectively. This facilitates a variety of new applications for related troughs and ridges to other meteorological variables such as cloud types, precipitation, warm conveyor belts or jet streams. The detection of the horizontal orientation allows for the grouping of troughs and ridges into cyclonic

---

[1] $1 \text{ pvu} = 10^{-6} \text{ m}^2 \text{ s}^{-1} \text{ K kg}^{-1}$

and anticyclonic categories. The tracking allows for the determination of the maturity of the troughs and ridges and how the orientation changes during the life cycle. Finally, the algorithm separates closed troughs from open troughs and ridges. The former are associated with one ore more closed geopotential isolines and are therefore related to upper-level lows or highs, which allows the possibility to connect them with surface low-pressure systems.

5   The second focus of this paper is on illustrating the performance of the detection using a case study and several climatological applications. These applications serve as stepping stones for future research. The general behavior of troughs and ridges is that both the trough and ridge detection frequencies are remarkably stationary, but regionally the picture can be complex. For example, during winter, troughs are most frequently detected downstream of the Rocky Mountains and over East Asia downstream of the Atlai-Sayan and Yablonoi mountain ranges, but they are much less frequently found downstream of Greenland,

10   where, in contrast, the ridge detection frequency is high. Thus, troughs are more transient or smaller in Greenland. Troughs are also frequent at the end of the Pacific storm track, but there is no comparable frequency maximum at the end of the Atlantic storm track during winter. Rather, a frequency maximum is located over East Europe, which is in contrast to summer, when there is a clear maximum at the end of the Atlantic storm track off the Iberian Peninsula (Fig. 3 and Fig. 4).

The horizontal orientation of troughs and ridges displays a strong meridional and longitudinal dependency. In general, over

15   the main oceanic storm tracks, troughs and ridges are cyclonically oriented, while they are oriented anticyclonically over land. The cyclonic orientation increases poleward, while the anticyclonic orientation increases equatorward. In agreement with earlier findings, which are based on traditional means to quantify the behavior of upper-level eddies (such as **E** vector), troughs and ridges are more cyclonically oriented over North America and the North Atlantic during El Niño-affected winter seasons. In contrast, these areas are more anticyclonically oriented during La Niña-affected winter seasons. Trough and ridge detection

20   thus provides complementary insights into the change in the dynamics of large-scale upper-level flow in response to external climate drivers. However, the orientation also exhibits a seasonal cycle, for example, during midwinter over the North Pacific when the Pacific jet moves equatorward. The subtropical jet creates a large-scale cyclonically sheared environment over the Pacific. Consequently, the troughs and ridges are during midwinter mostly cyclonic, and it is in particular the trough orientation that has a marked increase in cyclonic orientation, suggesting a potentially accelerated cyclone life cycle. These applications

25   give an indication for the usefulness of the novel detection method.

Finally, we explored the possibility of utilizing the detected troughs and ridges as starting points for parcel trajectories. Twenty-four-hour backward trajectories are released for two months (January and July 2010) from all the trough and ridge objects. For troughs, the distribution of 24-hour pressure changes along the flow is centered between 0 and 100 hPa, which reflects the isentropic downglide of equatorward moving air in a trough, with a long tail towards negative values (strong

30   ascent). For ridges, the distribution is consequently centered between -100 and 0 hPa, which reflects the isentropic upglide of poleward moving air in a ridge. Again, the distribution has a long tail towards negative values. During the summer, the tails of both distributions are reduced and strongly centered around small pressure changes of 50 hPa. If the distributions reflect mainly the mean isentropic motion of air masses in trough and ridge regions, then the strong confinement of the summer distributions near small pressure changes is due to the reduced baroclinicity. The corresponding distribution of PV changes is centered

35   around zero, with similar tails towards positive and negative values. Finally, the distribution of potential temperature changes

is centered around negative values (between -2 and $0\,\mathrm{K\,day}^{-1}$), with a long tail towards positive values. While the long tail reflects the heating during rapid cross-isentropic ascent, the mean and median indicates a mild loss potentially due to radiative cooling.

The presented tools offer new possibilities for studying the dynamics of upper-level wave development and associated
5   meteorological conditions at the surface or at the jet stream level. The application to climate data or century-long reanalysis data will allow for the analysis of long-term trends, extreme seasons or decadal variability in the frequency and orientation of troughs and ridges. The combination of the tool with Lagrangian diagnostics will allow for the development of a new three-dimensional perspective on trough and ridge development and for a quantification of the role of moist processes in shaping their life cycle.

10   *Code and data availability.* The monthly mean data will be made available at http://eraiclim.ethz.ch/. Higher resolution data can be provided upon request.

Author contributions. SeS and MS designed jointly the detection strategy. MS developed the algorithm. SeS performed the analyses. SeS and MS contributed equally to the interpretation and discussion of the results.

Competing interests. The authors declare no competing interests.

References

Afargan, H. and Kaspi, Y.: A Midwinter Minimum in North Atlantic Storm Track Intensity in Years of a Strong Jet, Geophysical Research Letters, 44, 12,511–12,518, https://doi.org/10.1002/2017GL075136, 2017.

Benedict, J. J., Lee, S., and Feldstein, S. B.: Synoptic View of the North Atlantic Oscillation, Journal of the Atmospheric Sciences, 61, 121–144, https://doi.org/10.1175/1520-0469(2004)061<0121:SVOTNA>2.0.CO;2, 2004.

Browning, K. A.: Conceptual Models of Precipitation Systems, Weather and Forecasting, 1, 23–41, https://doi.org/10.1175/1520-0434(1986)001<0023:CMOPS>2.0.CO;2, 1986.

Browning, K. A.: Organization of Clouds and Precipitation in Extratropical Cyclones, in: Extratropical cyclones, pp. 129–153, American Meteorological Society, Boston, MA, https://doi.org/10.1007/978-1-944970-33-8_8, 1990.

Chang, E. K. M.: GCM and Observational Diagnoses of the Seasonal and Interannual Variations of the Pacific Storm Track during the Cool Season, Journal of the Atmospheric Sciences, 58, 1784–1800, https://doi.org/10.1175/1520-0469(2001)058<1784:GAODOT>2.0.CO;2, 2001.

Chang, E. K. M. and Guo, Y.: Comments on "The Source of the Midwinter Suppression in Storminess over the North Pacific", Journal of Climate, 24, 5187–5191, https://doi.org/10.1175/2011JCLI3987.1, 2011.

Chang, E. K. M. and Guo, Y.: Is Pacific Storm-Track Activity Correlated with the Strength of Upstream Wave Seeding?, Journal of Climate, 25, 5768–5776, https://doi.org/10.1175/JCLI-D-11-00555.1, 2012.

Davies, H. C., Schär, C., and Wernli, H.: The Palette of Fronts and Cyclones within a Baroclinic Wave Development, Journal of the Atmospheric Sciences, 48, 1666–1689, https://doi.org/10.1175/1520-0469(1991)048<1666:TPOFAC>2.0.CO;2, 1991.

Dee, D. P., Uppala, S. M., Simmons, A. J., Berrisford, P., Poli, P., Kobayashi, S., Andrae, U., Balmaseda, M. A., Balsamo, G., Bauer, P., Bechtold, P., Beljaars, A. C. M., van de Berg, L., Bidlot, J., Bormann, N., Delsol, C., Dragani, R., Fuentes, M., Geer, A. J., Haimberger, L., Healy, S. B., Hersbach, H., Hólm, E. V., Isaksen, L., Kållberg, P., Köhler, M., Matricardi, M., McNally, A. P., Monge-Sanz, B. M., Morcrette, J.-J., Park, B.-K., Peubey, C., de Rosnay, P., Tavolato, C., Thépaut, J.-N., and Vitart, F.: The ERA-Interim reanalysis: configuration and performance of the data assimilation system, Quarterly Journal of the Royal Meteorological Society, 137, 553–597, https://doi.org/10.1002/qj.828, 2011.

Drouard, M., Rivière, G., and Arbogast, P.: The Link between the North Pacific Climate Variability and the North Atlantic Oscillation via Downstream Propagation of Synoptic Waves, Journal of Climate, 28, 3957–3976, https://doi.org/10.1175/JCLI-D-14-00552.1, 2015.

Franzke, C., Lee, S., and Feldstein, S. B.: Is the North Atlantic Oscillation a Breaking Wave?, Journal of the Atmospheric Sciences, 61, 145–160, https://doi.org/10.1175/1520-0469(2004)061<0145:ITNAOA>2.0.CO;2, 2004.

Graf, M. A., Wernli, H., and Sprenger, M.: Objective classification of extratropical cyclogenesis, Quarterly Journal of the Royal Meteorological Society, 143, 1047–1061, https://doi.org/10.1002/qj.2989, 2017.

Grams, C. M., Wernli, H., Böttcher, M., Čampa, J., Corsmeier, U., Jones, S. C., Keller, J. H., Lenz, C.-J., and Wiegand, L.: The key role of diabatic processes in modifying the upper-tropospheric wave guide: A North Atlantic case-study, Quarterly Journal of the Royal Meteorological Society, 137, 2174–2193, https://doi.org/10.1002/qj.891, 2011.

Gray, S. L. and Dacre, H. F.: Classifying dynamical forcing mechanisms using a climatology of extratropical cyclones, Quarterly Journal of the Royal Meteorological Society, 132, 1119–1137, https://doi.org/10.1256/qj.05.69, 2006.

Harnik, N. and Chang, E. K. M.: The Effects of Variations in Jet Width on the Growth of Baroclinic Waves: Implications for Midwinter Pacific Storm Track Variability, Journal of the Atmospheric Sciences, 61, 23–40, https://doi.org/10.1175/1520-0469(2004)061<0023:TEOVIJ>2.0.CO;2, 2004.

Harrold, T. W.: Mechanisms influencing the distribution of precipitation within baroclinic disturbances, Quarterly Journal of the Royal Meteorological Society, 99, 232–251, https://doi.org/10.1002/qj.49709942003, 1973.

Hoskins, B. J. and Hodges, K. I.: The Annual Cycle of Northern Hemisphere Storm Tracks. Part I: Seasons, Journal of Climate, 32, 1743–1760, https://doi.org/10.1175/JCLI-D-17-0870.1, 2019.

Hoskins, B. J., James, I. N., and White, G. H.: The Shape, Propagation and Mean-Flow Interaction of Large-Scale Weather Systems, Journal of the Atmospheric Sciences, 40, 1595–1612, https://doi.org/10.1175/1520-0469(1983)040<1595:TSPAMF>2.0.CO;2, 1983.

Lackmann, G. M., Keyser, D., and Bosart, L. F.: A Characteristic Life Cycle of Upper-Tropospheric Cyclogenetic Precursors during the Experiment on Rapidly Intensifying Cyclones over the Atlantic (ERICA), Monthly Weather Review, 125, 2729–2758, https://doi.org/10.1175/1520-0493(1997)125<2729:ACLCOU>2.0.CO;2, 1997.

Lee, S. and Feldstein, S.: Two Types of Wave Breaking in an Aquaplanet GCM, Journal of the Atmospheric Sciences, 53, 842–857, https://doi.org/10.1175/1520-0469(1996)053<0842:TTOWBI>2.0.CO;2, 1996.

Li, Y. and Lau, N.-C.: Impact of ENSO on the Atmospheric Variability over the North Atlantic in Late Winter—Role of Transient Eddies, Journal of Climate, 25, 320–342, https://doi.org/10.1175/JCLI-D-11-00037.1, 2012a.

Li, Y. and Lau, N.-C.: Contributions of Downstream Eddy Development to the Teleconnection between ENSO and the Atmospheric Circulation over the North Atlantic, Journal of Climate, 25, 4993–5010, https://doi.org/10.1175/JCLI-D-11-00377.1, 2012b.

Liu, Z. and Alexander, M.: Atmospheric bridge, oceanic tunnel, and global climatic teleconnections, Reviews of Geophysics, 45, https://doi.org/10.1029/2005RG000172, 2007.

Martius, O. and Rivière, G.: Rossby wave breaking: climatology, interaction with low-frequency climate variability, and links to extreme weather events, p. 69–78, Special Publications of the International Union of Geodesy and Geophysics, Cambridge University Press, https://doi.org/10.1017/CBO9781107775541.006, 2016.

Martius, O., Zenklusen, E., Schwierz, C., and Davies, H. C.: Episodes of Alpine heavy precipitation with an overlying elongated stratospheric intrusion: A climatology, International Journal of Climatology, 26, 1149–1164, https://doi.org/10.1002/joc.1295, 2006.

Martius, O., Schwierz, C., and Davies, H. C.: Tropopause-Level Waveguides, Journal of the Atmospheric Sciences, 67, 866–879, https://doi.org/10.1175/2009JAS2995.1, 2010.

Martius, O., Sodemann, H., Joos, H., Pfahl, S., Winschall, A., Croci-Maspoli, M., Graf, M., Madonna, E., Mueller, B., Schemm, S., Sedláček, J., Sprenger, M., and Wernli, H.: The role of upper-level dynamics and surface processes for the Pakistan flood of July 2010, Quarterly Journal of the Royal Meteorological Society, 139, 1780–1797, https://doi.org/10.1002/qj.2082, 2013.

Massacand, A. C., Wernli, H., and Davies, H. C.: Influence of upstream diabatic heating upon an Alpine event of heavy precipitation, Monthly Weather Review, 129, 2822–2828, https://doi.org/10.1175/1520-0493(2001)129<2822:IOUDHU>2.0.CO;2, 2001.

McIntyre, M. E. and Palmer, T.: Breaking planetary waves in the stratosphere, Nature, 305, 593, 1983.

Mo, K. C. and Livezey, R. E.: Tropical-Extratropical Geopotential Height Teleconnections during the Northern Hemisphere Winter, Monthly Weather Review, 114, 2488–2515, https://doi.org/10.1175/1520-0493(1986)114<2488:TEGHTD>2.0.CO;2, 1986.

Nakamura, H.: Midwinter Suppression of Baroclinic Wave Activity in the Pacific, Journal of the Atmospheric Sciences, 49, 1629–1642, https://doi.org/10.1175/1520-0469(1992)049<1629:MSOBWA>2.0.CO;2, 1992.

Nakamura, H. and Sampe, T.: Trapping of synoptic-scale disturbances into the North-Pacific subtropical jet core in midwinter, Geophysical Research Letters, 29, 8–1–8–4, https://doi.org/10.1029/2002GL015535, 2002.

Novak, L., Schneider, T., and Ait-Chaalal, F.: Midwinter suppression of storm tracks in an idealized zonally symmetric setting, Journal of the Atmospheric Sciences, 0, null, https://doi.org/10.1175/JAS-D-18-0353.1, 2020.

5 Orlanski, I.: Bifurcation in Eddy Life Cycles: Implications for Storm Track Variability, Journal of the Atmospheric Sciences, 60, 993–1023, https://doi.org/10.1175/1520-0469(2003)60<993:BIELCI>2.0.CO;2, 2003.

Orlanski, I. and Chang, E. K. M.: Ageostrophic Geopotential Fluxes in Downstream and Upstream Development of Baroclinic Waves, Journal of the Atmospheric Sciences, 50, 212–225, https://doi.org/10.1175/1520-0469(1993)050<0212:AGFIDA>2.0.CO;2, 1993.

Papritz, L. and Schemm, S.: Development of an idealised downstream cyclone: Eulerian and Lagrangian perspective on the kinetic energy,
10   Tellus A: Dynamic Meteorology and Oceanography, 65, 19 539, https://doi.org/10.3402/tellusa.v65i0.19539, 2013.

Penny, S., Roe, G. H., and Battisti, D. S.: The Source of the Midwinter Suppression in Storminess over the North Pacific, Journal of Climate, 23, 634–648, https://doi.org/10.1175/2009JCLI2904.1, 2010.

Penny, S. M., Roe, G. H., and Battisti, D. S.: Reply, Journal of Climate, 24, 5192–5194, https://doi.org/10.1175/2011JCLI4187.1, 2011.

Penny, S. M., Battisti, D. S., and Roe, G. H.: Examining Mechanisms of Variability within the Pacific Storm Track: Upstream Seeding and
15   Jet-Core Strength, Journal of Climate, 26, 5242–5259, https://doi.org/10.1175/JCLI-D-12-00017.1, 2013.

Petterssen, S. and Smebye, S. J.: On the development of extratropical cyclones, Quarterly Journal of the Royal Meteorological Society, 97, 457–482, https://doi.org/10.1002/qj.49709741407, 1971.

Pfahl, S., Schwierz, C., Croci-Maspoli, M., Grams, C. M., and Wernli, H.: Importance of latent heat release in ascending air streams for atmospheric blocking, Nature Geoscience, 8, 610–614, https://doi.org/10.1038/NGEO2487, 2015.

20 Pomroy, H. R. and Thorpe, A. J.: The Evolution and Dynamical Role of Reduced Upper-Tropospheric Potential Vorticity in Intensive Observing Period One of FASTEX, Monthly Weather Review, 128, 1817–1834, https://doi.org/10.1175/1520-0493(2000)128<1817:TEADRO>2.0.CO;2, 2000.

Postel, G. A. and Hitchman, M. H.: A Climatology of Rossby Wave Breaking along the Subtropical Tropopause, Journal of the Atmospheric Sciences, 56, 359–373, https://doi.org/10.1175/1520-0469(1999)056<0359:ACORWB>2.0.CO;2, 1999.

25 Raveh-Rubin, S. and Flaounas, E.: A dynamical link between deep Atlantic extratropical cyclones and intense Mediterranean cyclones, Atmospheric Science Letters, 18, 215–221, https://doi.org/10.1002/asl.745, 2017.

Rivière, G. and Orlanski, I.: Characteristics of the Atlantic Storm-Track Eddy Activity and Its Relation with the North Atlantic Oscillation, Journal of the Atmospheric Sciences, 64, 241–266, https://doi.org/10.1175/JAS3850.1, 2007.

Rivière, G., Hua, B. L., and Klein, P.: Perturbation growth in terms of barotropic alignment properties, Quarterly Journal of the Royal
30   Meteorological Society, 129, 2613–2635, https://doi.org/10.1256/qj.02.106, 2003.

Rüdisühli, S.: Attribution of Rain to Cyclones and Fronts Over Europe in a Kilometer-Scale Regional Climate Simulation, Ph.D. Thesis, ETH Zurich, p. 221pp, https://doi.org/10.3929/ethz-b-000351234, 2018.

Sanders, F.: Life History of Mobile Troughs in the Upper Westerlies, Monthly Weather Review, 116, 2629–2648, https://doi.org/10.1175/1520-0493(1988)116<2629:LHOMTI>2.0.CO;2, 1988.

35 Sanders, F. and Gyakum, J. R.: Synoptic-Dynamic Climatology of the "Bomb", Monthly Weather Review, 108, 1589–1606, https://doi.org/10.1175/1520-0493(1980)108<1589:SDCOT>2.0.CO;2, 1980.

Schemm, S.: Conveyor belts in idealized moist baroclinic wave life cycles, https://doi.org/10.3929/ethz-a-7632512, PhD Thesis, Dep. of Environmental Systems Science, ETH Zürich,190 pp., 2013.

Schemm, S. and Rivière, G.: On the Efficiency of Baroclinic Eddy Growth and How It Reduces the North Pacific Storm-Track Intensity in Midwinter, Journal of Climate, 32, 8373–8398, https://doi.org/10.1175/JCLI-D-19-0115.1, 2019.

Schemm, S. and Schneider, T.: Eddy Lifetime, Number, and Diffusivity and the Suppression of Eddy Kinetic Energy in Midwinter, Journal of Climate, 31, 5649–5665, https://doi.org/10.1175/JCLI-D-17-0644.1, 2018.

5 Schemm, S., Wernli, H., and Papritz, L.: Warm Conveyor Belts in Idealized Moist Baroclinic Wave Simulations, Journal of the Atmospheric Sciences, 70, 627–652, https://doi.org/10.1175/JAS-D-12-0147.1, 2013.

Schemm, S., Ciasto, L. M., Li, C., and Kvamstø, N. G.: Influence of Tropical Pacific Sea Surface Temperature on the Genesis of Gulf Stream Cyclones, Journal of the Atmospheric Sciences, 73, 4203–4214, https://doi.org/10.1175/JAS-D-16-0072.1, 2016.

Schemm, S., Rivière, G., Ciasto, L. M., and Li, C.: Extratropical Cyclogenesis Changes in Connection with Tropospheric ENSO Tele-
10 connections to the North Atlantic: Role of Stationary and Transient Waves, Journal of the Atmospheric Sciences, 75, 3943–3964, https://doi.org/10.1175/JAS-D-17-0340.1, 2018.

Simmons, A. J.: Numerical simulations of cyclone life cycles. Proceedings of an International Symposium on the Life Cycles of Extratropical Cyclones, vol. 1, Alma Mater Forlag, 1994.

Simmons, A. J. and Hoskins, B. J.: The Downstream and Upstream Development of Unstable Baroclinic Waves, Journal of the Atmospheric
15 Sciences, 36, 1239–1254, https://doi.org/10.1175/1520-0469(1979)036<1239:TDAUDO>2.0.CO;2, 1979.

Spreitzer, E., Attinger, R., Boettcher, M., Forbes, R., Wernli, H., and Joos, H.: Modification of Potential Vorticity near the Tropopause by Nonconservative Processes in the ECMWF Model, Journal of the Atmospheric Sciences, 76, 1709–1726, https://doi.org/10.1175/JAS-D-18-0295.1, 2019.

Sprenger, M. and Wernli, H.: The LAGRANTO Lagrangian analysis tool – version 2.0, Geoscientific Model Development, 8, 2569–2586,
20 https://doi.org/10.5194/gmd-8-2569-2015, https://www.geosci-model-dev.net/8/2569/2015/, 2015.

Sprenger, M., Fragkoulidis, G., Binder, H., Croci-Maspoli, M., Graf, P., Grams, C. M., Knippertz, P., Madonna, E., Schemm, S., Škerlak, B., and Wernli, H.: Global Climatologies of Eulerian and Lagrangian Flow Features based on ERA-Interim, Bulletin of the American Meteorological Society, 98, 1739–1748, https://doi.org/10.1175/BAMS-D-15-00299.1, 2017.

Stan, C., Straus, D. M., Frederiksen, J. S., Lin, H., Maloney, E. D., and Schumacher, C.: Review of Tropical-Extratropical Teleconnections
25 on Intraseasonal Time Scales, Reviews of Geophysics, 55, 902–937, https://doi.org/10.1002/2016RG000538, 2017.

Steinfeld, D. and Pfahl, S.: The role of latent heating in atmospheric blocking dynamics: a global climatology, Climate Dynamics, p. 1–22, https://doi.org/10.1007/s00382-019-04919-6, 2019.

Stoelinga, M. T.: A Potential Vorticity-Based Study of the Role of Diabatic Heating and Friction in a Numerically Simulated Baroclinic Cyclone, Monthly Weather Review, 124, 849–874, https://doi.org/10.1175/1520-0493(1996)124<0849:APVBSO>2.0.CO;2, 1996.

30 Thorncroft, C. D., Hoskins, B. J., and McIntyre, M. E.: Two paradigms of baroclinic-wave life-cycle behaviour, Quarterly Journal of the Royal Meteorological Society, 119, 17–55, https://doi.org/10.1002/qj.49711950903, 1993.

Trenberth, K. E.: An Assessment of the Impact of Transient Eddies on the Zonal Flow during a Blocking Episode Using Localized Eliassen-Palm Flux Diagnostics, Journal of the Atmospheric Sciences, 43, 2070–2087, https://doi.org/10.1175/1520-0469(1986)043<2070:AAOTIO>2.0.CO;2, 1986.

35 Uccellini, L. W.: Processes contributing to the rapid development of extratropical cyclones, in: Extratropical cyclones, pp. 81–105, American Meteorological Society, Boston, MA, https://doi.org/10.1007/978-1-944970-33-8_6, 1990.

Wash, C. H., Peak, J. E., Calland, W. E., and Cook, W. A.: Diagnostic Study of Explosive Cyclogenesis during FGGE, Monthly Weather Review, 116, 431–451, https://doi.org/10.1175/1520-0493(1988)116<0431:DSOECD>2.0.CO;2, 1988.

Wernli, B. H. and Davies, H. C.: A lagrangian-based analysis of extratropical cyclones. I: The method and some applications, Quarterly Journal of the Royal Meteorological Society, 123, 467–489, https://doi.org/10.1002/qj.49712353811, 1997.

Wernli, H.: A lagrangian-based analysis of extratropical cyclones. II: A detailed case-study, Quarterly Journal of the Royal Meteorological Society, 123, 1677–1706, https://doi.org/10.1002/qj.49712354211, 1997.

5   Wernli, H. and Schwierz, C.: Surface Cyclones in the ERA-40 Dataset (1958–2001). Part I: Novel Identification Method and Global Climatology, Journal of the Atmospheric Sciences, 63, 2486–2507, https://doi.org/10.1175/JAS3766.1, 2006.

Wernli, H. and Sprenger, M.: Identification and ERA-15 Climatology of Potential Vorticity Streamers and Cutoffs near the Extratropical Tropopause, Journal of the Atmospheric Sciences, 64, 1569–1586, https://doi.org/10.1175/JAS3912.1, 2007.

Wernli, H., Dirren, S., Liniger, M. A., and Zillig, M.: Dynamical aspects of the life cycle of the winter storm 'Lothar' (24–26 December

10   1999), Quarterly Journal of the Royal Meteorological Society, 128, 405–429, https://doi.org/10.1256/003590002321042036, 2002.

Yeh, S.-W., Cai, W., Min, S.-K., McPhaden, M. J., Dommenget, D., Dewitte, B., Collins, M., Ashok, K., An, S.-I., Yim, B.-Y., and Kug, J.-S.: ENSO Atmospheric Teleconnections and Their Response to Greenhouse Gas Forcing, Reviews of Geophysics, 56, 185–206, 2018.

Yuval, J., Afargan, H., and Kaspi, Y.: The Relation Between the Seasonal Changes in Jet Characteristics and the Pacific Midwinter Minimum in Eddy Activity, Geophysical Research Letters, 45, 9995–10 002, https://doi.org/10.1029/2018GL078678, 2018.
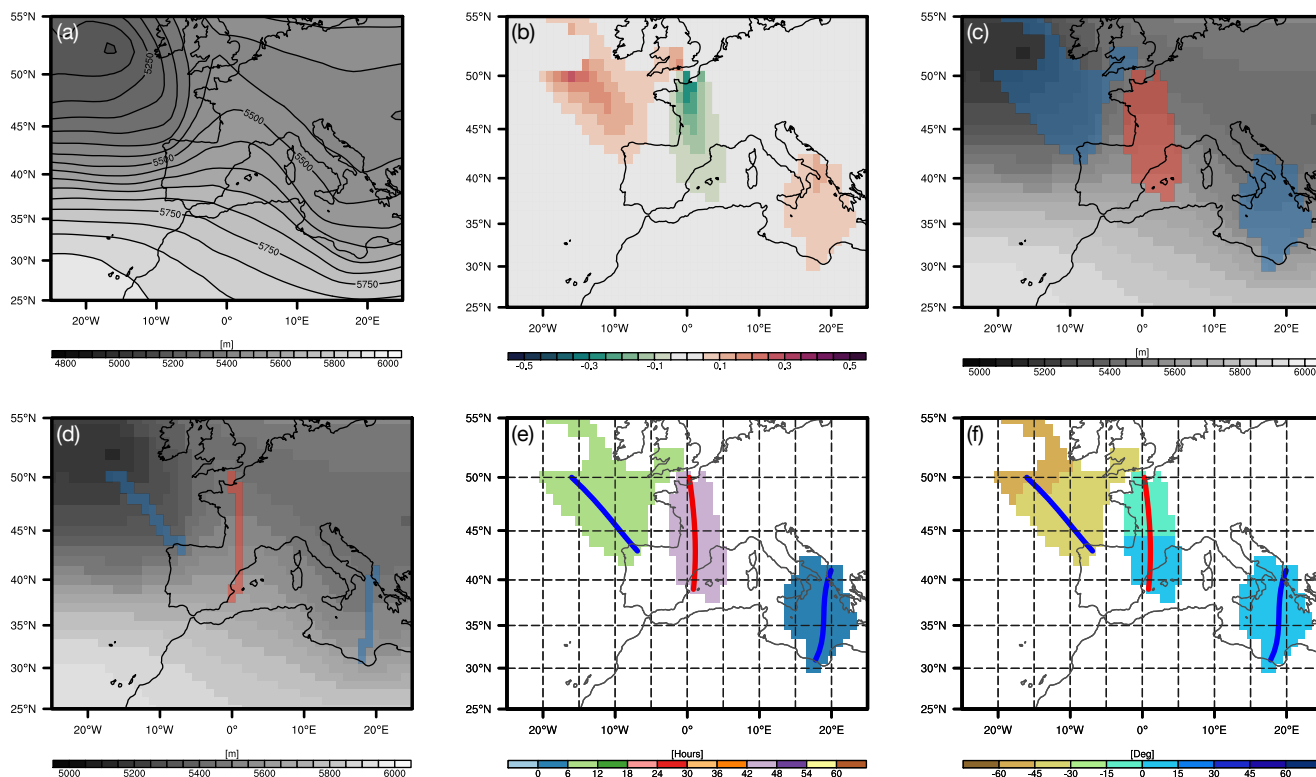
Figure 1. (a) 500-hPa geopotential height (m) at 12 UTC on 12 January 2010, (b) curvature of the geopotential isolines (units: degrees per kilometer) on the $1° \times 1°$ input grid at every grid point where the curvature is larger than 0.05 degrees per km; (c) 2D trough (blue) and ridge (red) masks and geopotential height (gray shading) at every grid point; (d) Corresponding trough (blue) and ridge (red) axes; (e) Cubic-spline interpolated trough and ridge axes and age (color; in hours) of the trough and ridge features; (f) Horizontal orientation of the trough and ridge object (in degrees; angle relative to a north-south meridian and estimated from the corresponding axis).
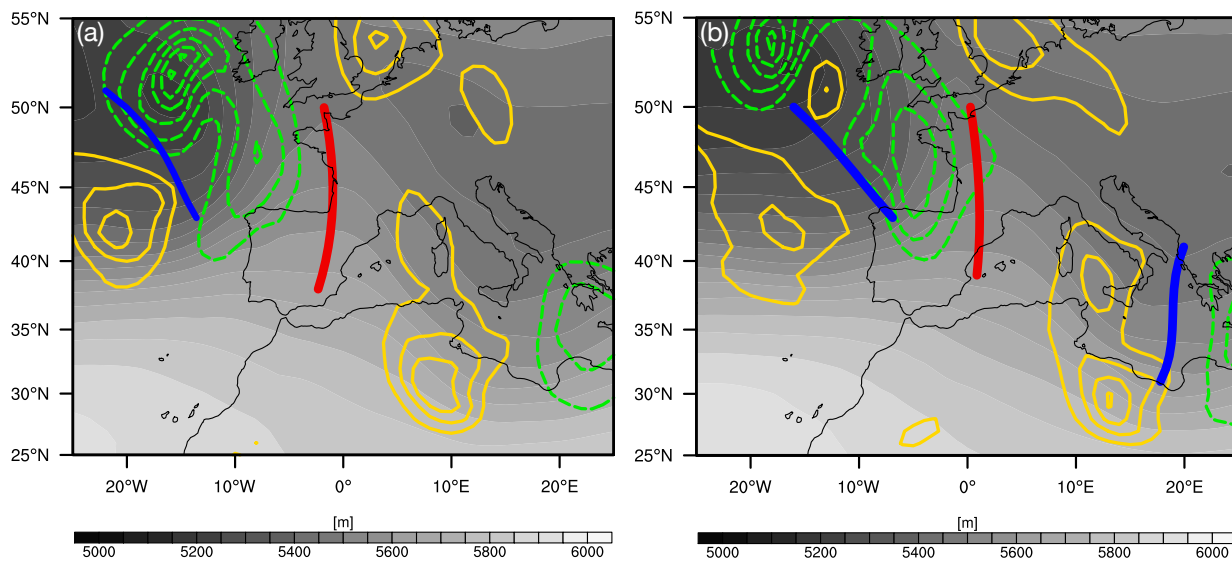
Figure 2. 500-hPa trough (blue) and ridge (red) axes at (a) 06 UTC and (b) 12 UTC on 12 January 2010, quasi-geostrophic omega (from 0.1 to 1 in steps of 0.1 m s^{-1}; positive values in yellow indicate descent and negative values in green indicate ascent) and geopotential height (m; gray shading).
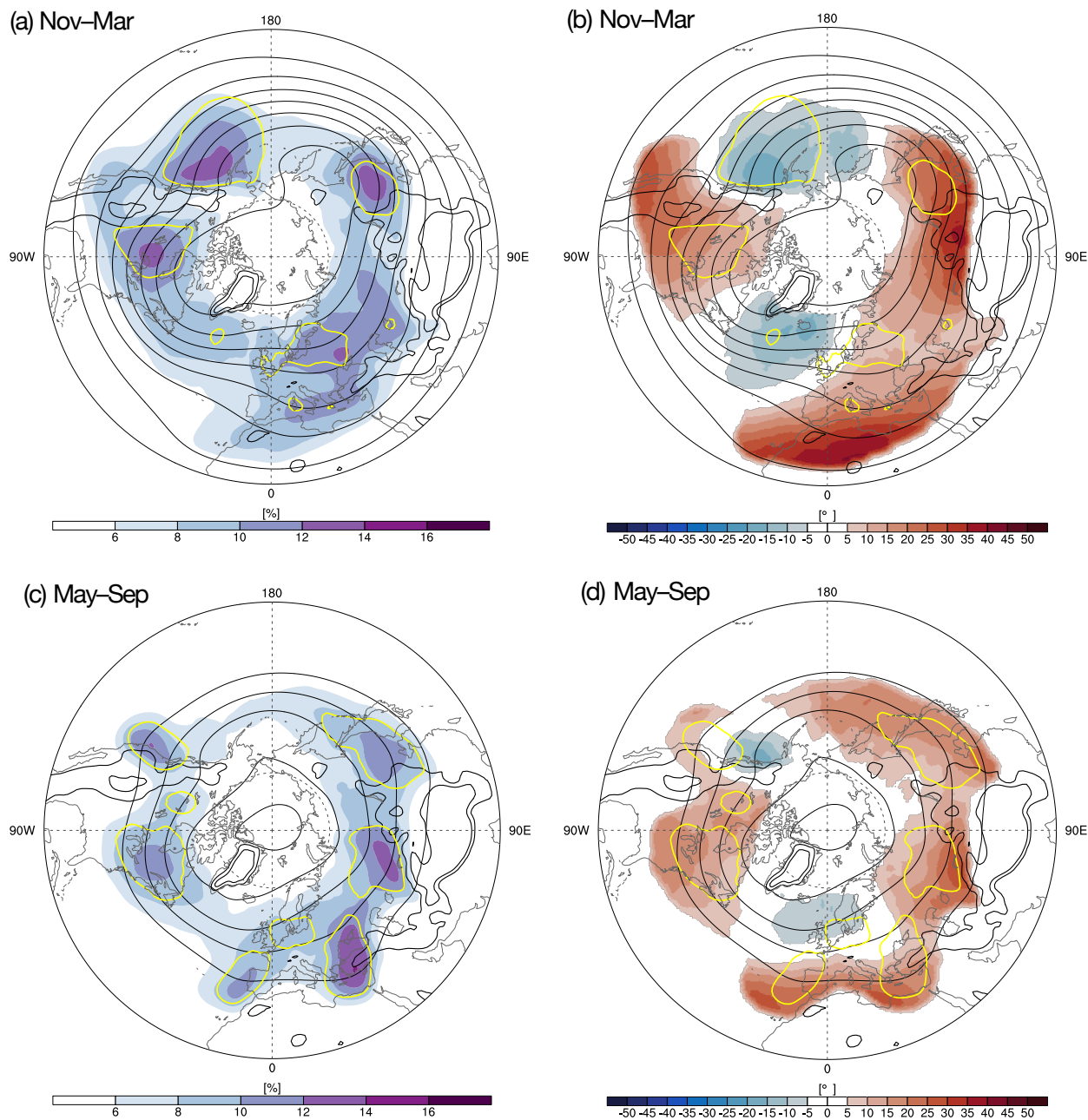
Figure 3. Left column: Seasonal climatologies of the trough detection frequencies (color shading; units: %) for the cold (a; Nov–Mar) and warm (c; May–Sep) seasons. Additional contours show selected frequencies of troughs with an age between 0 and 24 hours (yellow). Right column: Seasonal climatologies of the corresponding horizontal trough orientation on the 500-hPa level (color shading; units: degrees) for the cold (b; Nov–Mar) and warm (d; May–Sep) seasons,. Positive values indicate anticyclonically oriented troughs. Additionally, the yellow 0–24-hour age contour, similar to that in (a, c), is shown for reference. The 1,500-m height contour (black) is shown in all the panels.
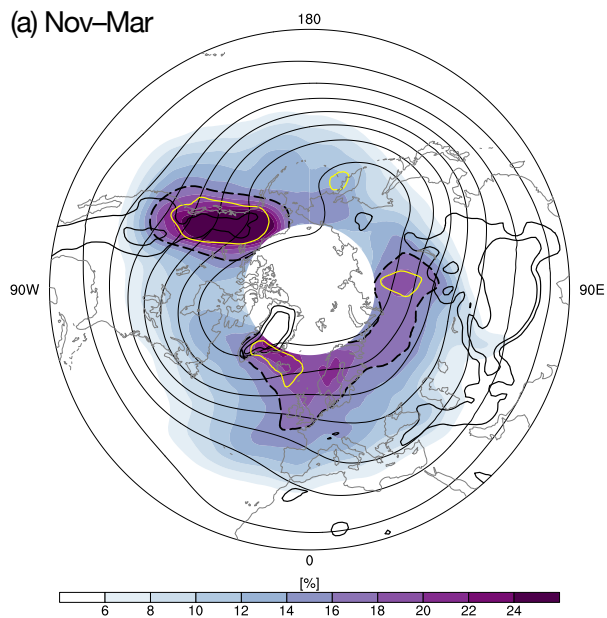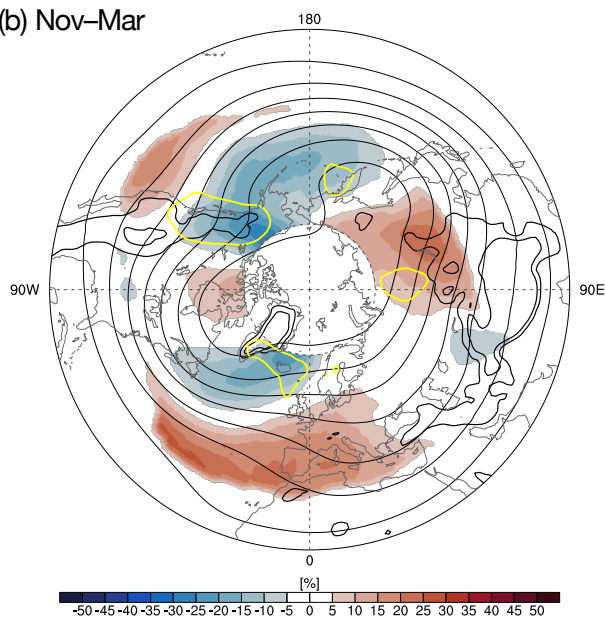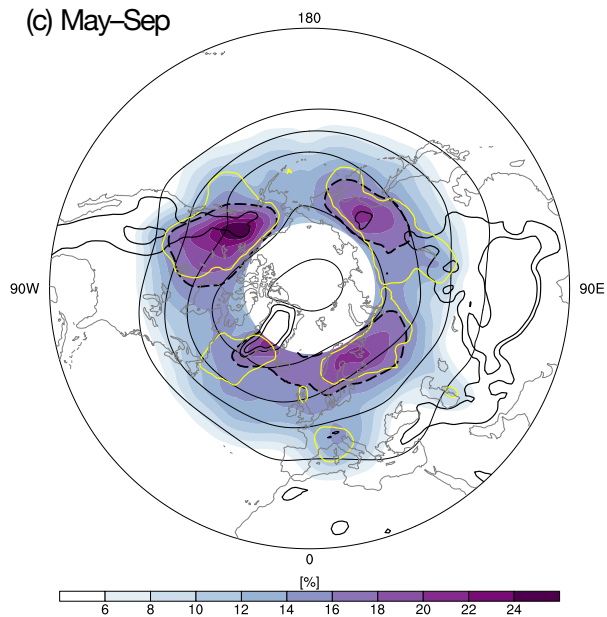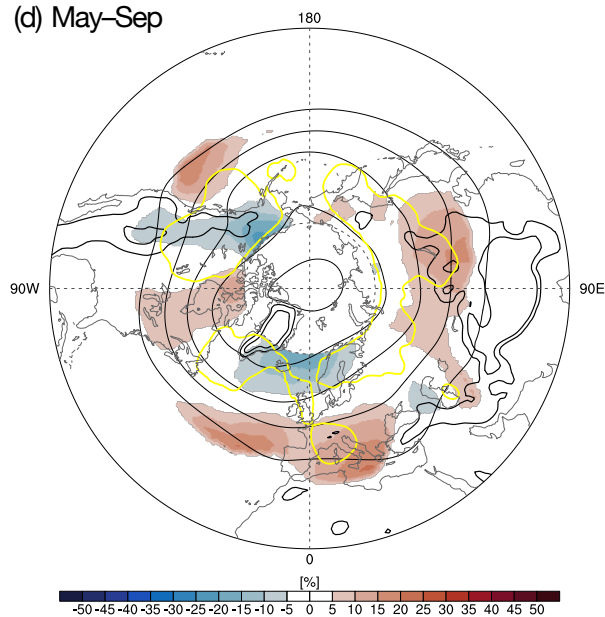
Figure 4. Similar to Fig. 3 but for ridges. The dashed contour indicates the region where the ridge frequency is above the maximum global trough detection frequency ($\approx 16\,\%$).

(a) El Niño
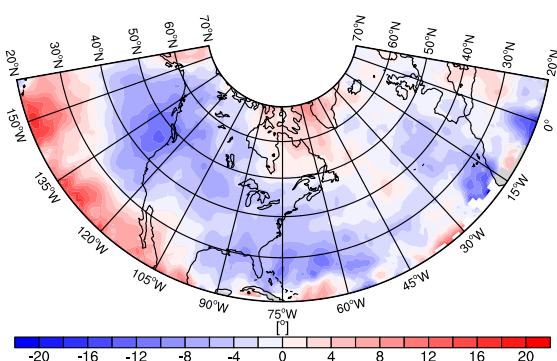
(b) La Niña
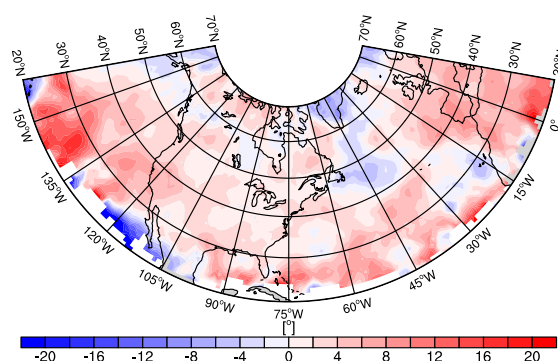
Figure 5. Averaged orientation anomalies (units: degrees) of 500-hPa troughs and ridges during (a) El Niño- and (b) La Niña-affected winter seasons. (Positive) Negative anomalies indicate more (anti)cyclonically oriented troughs and ridges compared to the seasonal climatology.
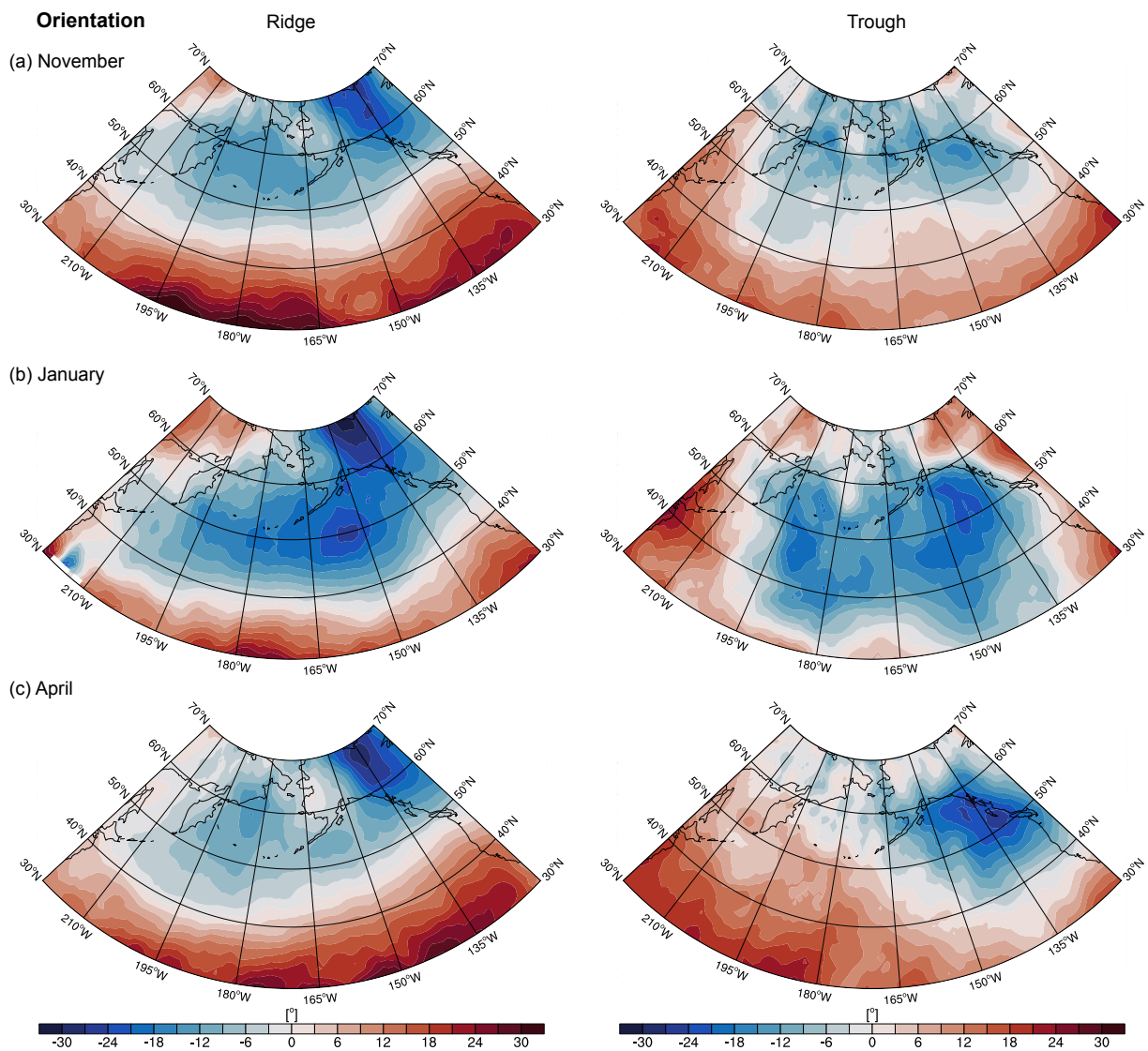
Figure 6. Monthly mean orientation (degrees) of 500-hPa ridges and troughs during (a) October, (b) January and (c) April over the North Pacific.
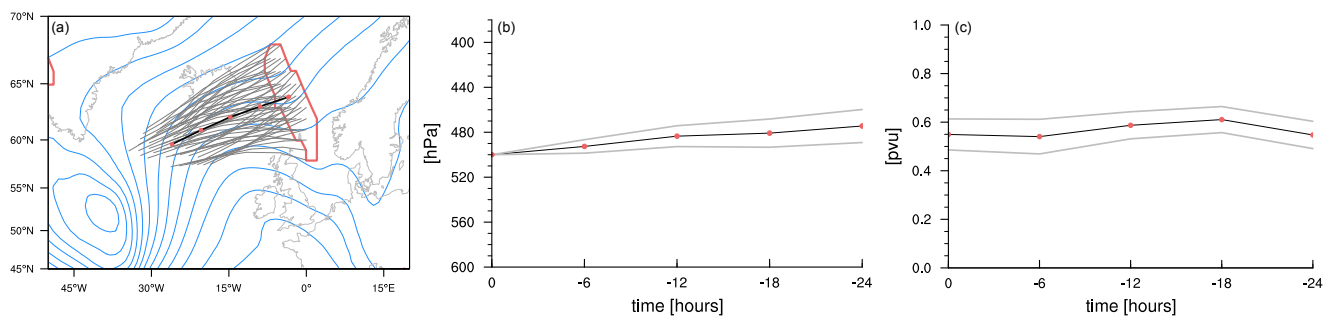
Figure 7. (a) Twenty-four-hour backward trajectories (gray lines) released from a trough feature (red contours) at 500 hPa. The black contour indicates the average over all the trajectories. Red dots indicate 6-hourly time steps. Geopotential heights are shown as blue contours (5000 to 5600 m in steps of 50 m). (b) Mean pressure evolution (black; hPa) along the backward trajectories shown in (a). The standard deviation across the sample is indicated by thin gray lines. Red dots denote 6-hour steps. (c) Similar to (b) but for the potential vorticity (pvu).
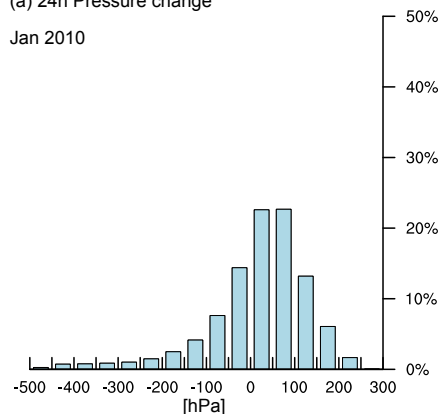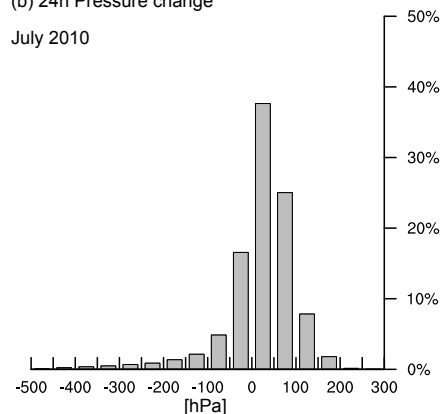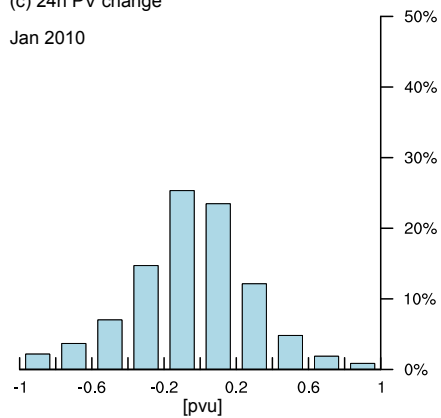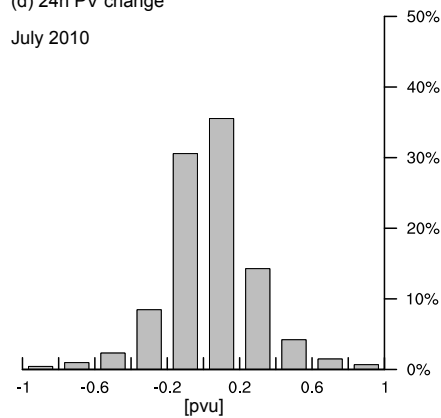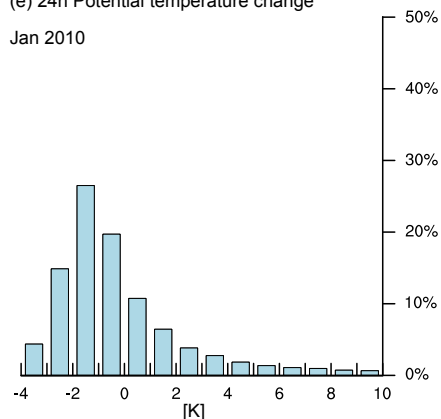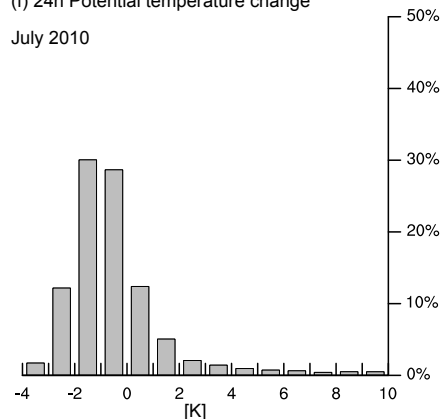
Figure 8. Histograms of the change (a, b) in pressure (hPa day^{-1}), (c, d) the potential vorticity (pvu day^{-1}) and (e, f) potential temperature (K day^{-1}) along the flow of parcel trajectories released from all troughs detected at the 500-hPa level during (a, c) January and (b, d) July 2010.
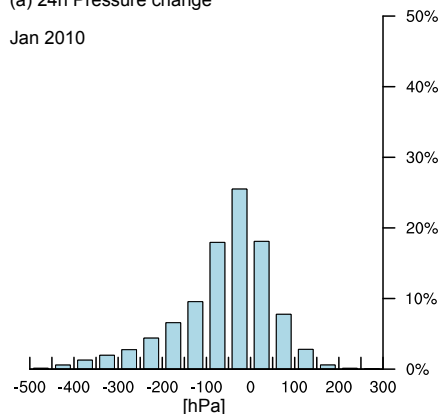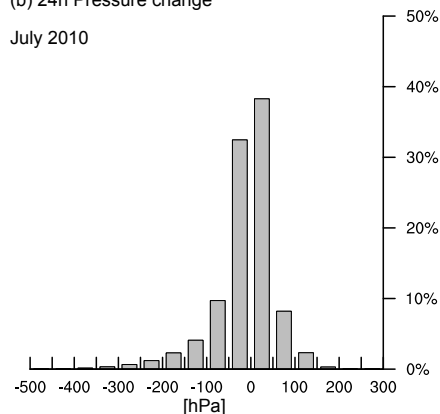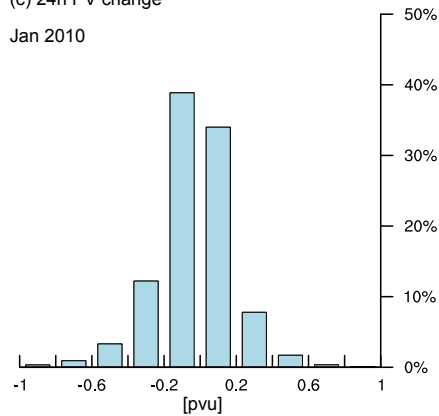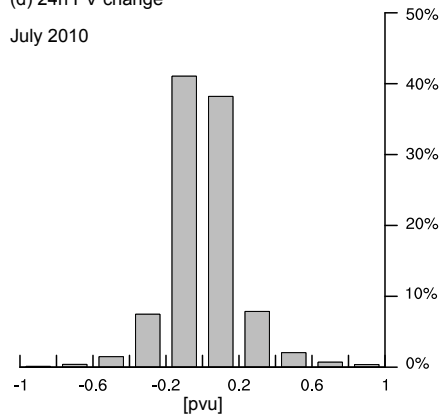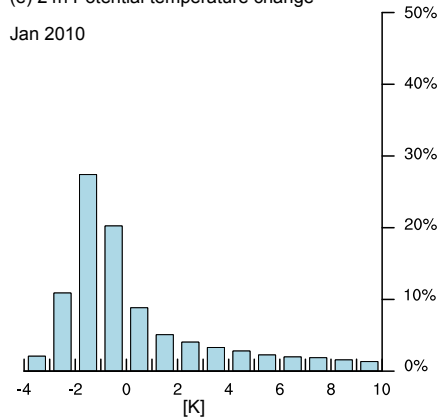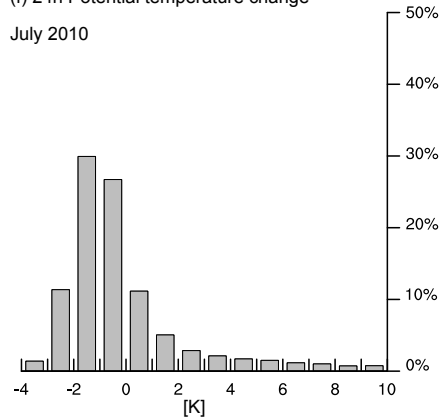
Figure 9. Similar to Fig. 8 but for 500-hPa ridges.